PHYSICAL REVIEW E **82**, 056408 (2010)

Hydrodynamic study of plasma amplifiers for soft-x-ray lasers: A transition in hydrodynamic behavior for plasma columns with widths ranging from 20 μm to 2 mm

Eduardo Oliva,[1,2,*] Philippe Zeitoun,[2] Pedro Velarde,[1] Marta Fajardo,[3] Kevin Cassou,[4] David Ros,[4] Stephan Sebban,[2]
David Portillo,[1] and Sebastien le Pape[5]
[1]*Instituto de Fusión Nuclear, Universidad Politécnica de Madrid, 28006 Madrid, Spain*
[2]*Laboratoire d'Optique Apliquée, ENSTA ParisTech, École Polytechnique, CNRS UMR 7639, 91761 Palaiseau Cedex, France*
[3]*Instituto de Plasmas e Fusão Nuclear, Instituto Superior Técnico, 1049-001 Lisbon, Portugal*
[4]*Laboratoire de Physique des Gaz et des Plasmas, UMR 8578, CNRS–Université Paris Sud XI, 91405 Orsay Cedex, France*
[5]*Lawrence Livermore National Laboratory, Livermore, California 94551, USA*

(Received 5 August 2010; published 12 November 2010)

Plasma-based seeded soft-x-ray lasers have the potential to generate high energy and highly coherent short pulse beams. Due to their high density, plasmas created by the interaction of an intense laser with a solid target should store the highest amount of energy density among all plasma amplifiers. Our previous numerical work with a two-dimensional (2D) adaptive mesh refinement hydrodynamic code demonstrated that careful tailoring of plasma shapes leads to a dramatic enhancement of both soft-x-ray laser output energy and pumping efficiency. Benchmarking of our 2D hydrodynamic code in previous experiments demonstrated a high level of confidence, allowing us to perform a full study with the aim of the way for 10–100 μJ seeded soft-x-ray lasers. In this paper, we describe in detail the mechanisms that drive the hydrodynamics of plasma columns. We observed transitions between narrow plasmas, where very strong bidimensional flow prevents them from storing energy, to large plasmas that store a high amount of energy. Millimeter-sized plasmas are outstanding amplifiers, but they have the limitation of transverse lasing. In this paper, we provide a preliminary solution to this problem.

DOI: 10.1103/PhysRevE.82.056408 PACS number(s): 42.55.Vc, 52.59.Ye, 52.65.−y

I. INTRODUCTION

There is much interest in developing bright sources of coherent soft-x-ray radiation. Free-electron lasers (FELs), seeded plasma-based soft-x-ray lasers, and high harmonics are currently available for applications in various fields ranging from biology [1] to physics [2]. However, many breakthrough experiments envisaged today are demonstrated only with FEL since they require an energy per pulse exceeding 10 μJ to produce ultrahigh intensities [3] near or above 10^{16} W/cm^2 to perform single-shot images [4] of samples evolving on the femtosecond time scale. Within the panorama of intense soft-x-ray sources, plasma-based soft-x-ray lasers are very attractive since they demonstrate the highest energy per pulse, up to 10 mJ [5]. However, these lasers are derived from a weakly coherent source, emitting hundred picosecond pulses. Their long pulse duration and poor optical qualities prevent them from being used in the most exacting applications. Seeding a plasma amplifier with high harmonics radiation [6–12] is a promising way to obtain sources with the required temporal and optical parameters, as the advantages of high harmonics radiation (shorter pulses, good wave front, and spatial coherence) can be mixed with the high energy output of soft-x-ray lasers [5].

The first seeding experiment was reported in 1995 by Ditmire and co-workers [6]. Although amplification of the harmonic pulse was observed, the saturation regime was not achieved. In addition to this, the background plasma emission was of the same order of magnitude of the amplified harmonics. Saturation was achieved in 2004 by the team leaded by Zeitoun [7]. The harmonic beam was focused into a gas amplifier to seed a high intensity beam. As expected, seeding experiments achieved with gas amplifiers demonstrated high quality beams with a high degree of coherence that were fully polarized [7] and had a diffraction-limited wave front [13]. However, the pulse duration was estimated to be long at around 5 ps. The energy was measured to be around 1 μJ per pulse [7]. Since amplifiers based on solid targets are denser than those generated from gas, higher-energy and shorter pulse durations were expected. However, experiments demonstrated lower energies of around 90 nJ and slightly shorter pulse durations down to 1 ps [12]. Our recent theoretical study explained the reason why the pulse duration was still in the picosecond range and provides a method for achieving 100 fs and shorter pulses [14]. We thus concentrated this study on the understanding of the mismatch between expected and measured energies for solid targets with the goal of finding a way to produce a seeded plasma-based soft-x-ray laser emitting energies of tens of microjoules per pulse, as required by many applications.

We would like to emphasize that in this paper, we consider only the case of seeded soft-x-ray lasers [7,8] since only this type of laser demonstrates a highly coherent, polarized, diffraction-limited beam. Therefore, we assume that only one train of soft-x-ray lasers has been amplified, which allows us to directly estimate the output energy from the plasma parameters (gain and saturation fluence). Following the studies in [15,16], the plasma parameters were calculated using a sophisticated hydrodynamic code called ARWEN [17]. To our knowledge, ARWEN is the only code used for modeling soft-x-ray lasers in two-dimensional (2D) geometry with

---

[*] eduardo.oliva@ensta-paristech.fr

radiation transfer based on the recent technique of adaptive mesh refinement (AMR). It allows for a very realistic plasma description but, thanks to the AMR technique, the computing time is quite low compared to that of non-AMR 2D codes. The hydrodynamic parameters are postprocessed with a simple three-level atomic model [15] to obtain 2D maps of several data, such as peak gain and saturation fluence among others. The layout of this paper is as follows. In Sec. II A, we present the computational tools (ARWEN code is presented in Sec. II A and the postprocessor is presented in Sec. II B). In Sec. III, we describe the initial parameters of the model (target and laser shapes and laser time structure). In Sec. IV, we present the results for plasmas created by lasers focused into lines with widths ranging from 20 μm to 1 mm. We discuss how the plasma evolution over time impacts gain (peak value and shape). In Sec. V, we estimate, based on a simple propagation model, the output energy of a seeded soft-x-ray laser. Finally, consequent to the emergence of large-scale short pulse lasers (Colorado State University laser, LASERIX [18,19], ILE in France, and ELI in Europe), we consider it important to investigate the 100 μJ frontier for seeded soft-x-ray lasers. In Sec. VI, we show a preliminary study of amplification in very large plasmas. We demonstrate that transverse lasing is a deleterious competing effect and present a solution to overcome it. Finally, in Sec. VII, we present our major conclusions and propose directions for building very high energy (tenths of millijoules between $\lambda \approx 3$ nm and $\lambda \approx 60$ nm) soft-x-ray lasers in the future.

II. COMPUTATIONAL TOOLS

Our major tool for this study is the ARWEN code [17]. This code has been used in several fields, such as those involving inertial confinement fusion [20], laboratory astrophysics [21], and plasma-based seeded soft-x-ray lasers [15,16], and thus has been thoroughly benchmarked. The simple atomic level code was originally written for [15] and has been modified in studies presented in [15,16] to facilitate postprocessing of the ARWEN data.

A. ARWEN code

The ARWEN code is a 2D hydrodynamic code incorporating radiation transport that was developed at the Instituto de Fusión Nuclear of the Universidad Politécnica de Madrid, Spain. The equations solved are those of radiation hydrodynamics with thermal conduction,

$$\frac{\partial \rho}{\partial t} + \nabla \cdot (\rho \mathbf{u}) = 0, \tag{1}$$

$$\frac{\partial \rho \mathbf{u}}{\partial t} + \nabla \cdot (\rho \mathbf{u}\mathbf{u}) = -\nabla(\mathbf{P_m} + \mathbf{P_r}), \tag{2}$$

$$\frac{\partial \rho E_m}{\partial t} + \nabla \cdot [\rho E_m \mathbf{u} + (\mathbf{P_m} + \mathbf{P_r})\mathbf{u}] = S_E + \nabla \cdot \mathbf{q_c} + \nabla \cdot \mathbf{q_r}, \tag{3}$$

$$\mathbf{\Omega} \cdot \nabla \mathbf{I} + \kappa \cdot \mathbf{I} = \epsilon, \tag{4}$$

$$\nabla \cdot \mathbf{q_c} = -\nabla \cdot \mathbf{k_e} \nabla \mathbf{T}, \tag{5}$$

$$\nabla \cdot \mathbf{q_r} = \int (\kappa \cdot \mathbf{I} - \epsilon) \mathbf{d}\nu, \tag{6}$$

$$E_r = \frac{1}{c}\int I d\mathbf{\Omega} d\nu, \tag{7}$$

$$P_r = \tfrac{1}{3} E_r, \tag{8}$$

where ρ is the density, $\mathbf{u}$ is the velocity vector, P_m and P_r are, respectively, the matter and radiation pressure tensors, E_m is the energy of the matter, S_E is the laser energy source, $\mathbf{q_c}$ and $\mathbf{q_r}$ are, respectively, the heat fluxes due to conduction and radiation, c is the light celerity, I is the radiation intensity, Ω is the solid angle, κ and ϵ are, respectively, the opacity and the emissivity of the medium, k_e is the thermal conductivity, ν is the frequency of the radiation, and E_r is the energy of the radiation field.

The Navier-Stokes equations [Eqs. (1)–(3)], including radiation pressure P_r and radiation heat transfer $\mathbf{q_r}$, are solved with an Eulerian scheme using a high-order Godunov type method with an approximate Riemann solver based on [22]. Flux-limited thermal electron conduction (5) and radiation transport (4) and (6) are treated with multigrid [23] and S_n multigroup methods [24,25], respectively. Matrix-free solvers for thermal conduction are available in the new version of the code.

Laser energy deposition is treated with a simple model as explained later in this paper. The laser energy is treated as a source term for Eq. (5). Planar and cylindrical geometries are available.

Equations of state data are obtained from the QEOS [26] equation of state, and the multipliers are adjusted to fit experimental data as the Hugoniot curves. Opacities are computed with JIMENA [27] code, also developed at the Instituto de Fusión Nuclear.

The ARWEN code (and thus all its packages) is based on the adaptive mesh refinement technique [28,29]. It is common in plasma hydrodynamics simulations to have small zones where high resolution is needed (i.e., shockwaves or high-energy zones), whereas the majority of the computational domain is well resolved with coarser grids. The AMR technique consists of putting patches of finer grids where they are needed, producing a uniform numerical error and saving computational time. The structure of levels and grids is created and controlled by the C++ library BoxLib [30].

The output of the code is in both our native format (rwm) and also the standard HDF format to facilitate postprocessing with other codes, such as our atomic model or codes that model the injection and amplification of radiation in the plasma, such as SHADOX [31].

B. Atomic model

The hydrodynamic parameters obtained from ARWEN were postprocessed to obtain 2D maps of atomic data as small-signal gain (which we will call "gain" in the rest of the paper) and saturation fluence among others. This postprocessing is done with a simple three-level atomic model that computes the gain and saturation fluence on the $2p^5_{1/2}3s_{1/2}$, $J=1\rightarrow 2p^5_{1/2}3p_{1/2}$, $J=0$ neonlike Fe^{16+} transition occurring at $\lambda=25.5$ nm. This calculation slightly overestimates the gain [32]. In our model, we follow the classical assumption that assumes that the fundamental level 0 is much more populated than the other two levels. There is a forbidden transition between the fundamental level and the upper lasing level 2. The lower lasing level 1 depopulates quickly toward the fundamental level 0, creating a population inversion between the two lasing levels 1 and 2 by collisional excitation, as shown in [33]. This phenomenon was confirmed later in [34], demonstrating that for the high temperatures that typically exist in transient collisional excitation [35], collisional excitation is the dominant process populating the laser levels.

The objective of the model is to compute the small-signal gain coefficient $g_0(\nu=\nu_0)$ and saturation fluence $F_{sat}(\nu=\nu_0)$ at the lasing line central frequency ν_0. For simplicity of notation, we will later use $g_0(0)$ and $F_{sat}(0)$,

$$g_0(\nu=\nu_0)=\left(N_2-\frac{\gamma_2}{\gamma_1}N_1\right)\sigma_{stim}(\nu=\nu_0), \tag{9}$$

$$F_{sat}(\nu=\nu_0)=\frac{h\nu_0}{\sigma_{stim}(\nu=\nu_0)}. \tag{10}$$

In these formulas, N_i and γ_i are, respectively, the population and degeneracy of the ith level of the transition and σ_{stim} is the stimulated emission cross-section. These last four values are computed at the line center. The populations of the levels are computed by solving the stationary rate equations of our three-level model,

$$\frac{dN_i}{dt}=\sum_j C_{ij}n_eN_j+\sum_j A_{ij}N_i, \tag{11}$$

$$\frac{dN_i}{dt}=0, \tag{12}$$

where the C_{ij} are the collisional excitation rates between levels i and j, the A_{ij} are the spontaneous emission and absorption coefficients, the N_i are the populations of the corresponding level i, and n_e is the electron density. The plus or minus sign is included in the coefficients depending on the effect of the transition (populating or depopulating level i).

The upper (numbered 2) and lower (numbered 1) lasing levels are $2p^5_{1/2}3p_{1/2}$ $J=0$ and $2p^5_{1/2}3s_{1/2}$ $J=1$, respectively. The fundamental level (numbered 0) is $2p^6$ $J=0$. The mechanisms taken into account in our model are collisional excitation between the fundamental and the two lasing levels ($0\rightarrow 2$, $0\rightarrow 1$), collisional de-excitation, and radiative transitions ($2\rightarrow 1$, $1\rightarrow 0$). Electron collisional rates are Van Regemorter's rates [38], which depend on the electron temperature (computed as explained above) and electron density (also given by our code). The rates are calculated assuming that the electrons have a Maxwellian distribution of velocities,

$$C_{ij}\approx 1.6\times 10^{-5}\frac{f_{ij}\langle g\rangle}{\Delta E_{ij}\cdot\sqrt{kT_e}}e^{-\Delta E_{ij}/kT_e}, \tag{13}$$

$$C_{ji}\approx\frac{\gamma_i}{\gamma_j}C_{ij}\cdot e^{\Delta E_{ij}/kT_e}, \tag{14}$$

where f_{ij} is the oscillator strength, $\langle g\rangle$ is the Gaunt factor (assumed to be $\langle g\rangle=0.2$), ΔE_{ij} is the difference of energy between levels i and j, k is Boltzmann's constant, and T_e is the electron temperature.

The stimulated emission cross section is computed as follows:

$$\sigma_{stim}(\nu)=\Phi(\nu)\frac{\lambda^2}{8\pi}A_{21}, \tag{15}$$

where A_{21} is Einstein's coefficient of the $2\rightarrow 1$ transition and $\Phi(\nu)$ is the spectral line profile. We assume only a Doppler profile. Neglecting collisional broadening reduces the profile width, artificially augmenting the gain and underestimating the saturation fluence [14], as shown in [37].

The Doppler effect is the principal mechanism of line broadening. In addition to this, we computed the value of the gain at the center of the line profile. Then, the peak Doppler value is

$$\Phi_D(0)=\lambda\left(\frac{m}{2\pi kT_i}\right)^{1/2}, \tag{16}$$

where m is the atomic mass of the lasing ions, k is Boltzmann's constant, and T_i is the ion temperature.

These simulations of transient collisional excitation pumping, using a combination of a long nanosecond pulse and a short picosecond pulse, were performed with a one-temperature hydrodynamic version of the ARWEN code. During the interaction of the long pulse with the plasma, both electron and ion fluids have enough time to thermalize through collisions. This assumption has been validated in several experiments and modeling of plasmas heated with nanosecond pulses. However, the peak gain appears only after interaction with the picosecond pulse when the electron temperature has been dramatically increased, while the ion temperature still remained nearly unchanged. Consequently, we calculated the gain at the instant of the peak value using the ion temperature before the interaction with the short pulse and the electron temperature as the value given by ARWEN at the moment of the pulse interaction.

III. PARAMETERS OF THE SIMULATIONS

Recently, modeling efforts aimed at optimizing the amplification region have been published [15] and have led to the conclusion that 2D effects, driven by the transverse spatial laser profile, have a strong impact on plasma hydrodynamics. Compared to a classical Gaussian profile, a super-Gaussian profile enlarges the gain zone surface and reduces the transverse refraction as energy deposition along the transverse direction (X axis) enhances laser coupling to the plasma and reduces energy loss due to lateral plasma cooling.

Having optimized the laser profile, we conducted simulations to study the influence of the focal width on plasma

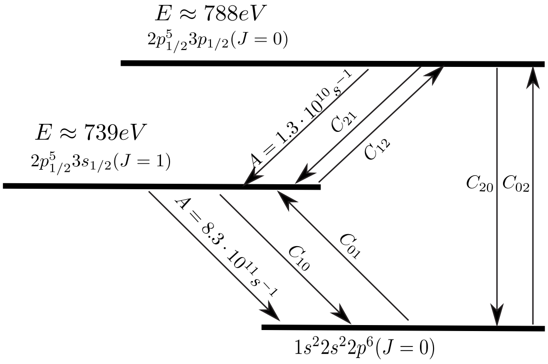

FIG. 1. Simplified Grotrian scheme and transitions obtained from [36,37] for Ne-like Fe.

hydrodynamics. We simulated amplifiers pumped by a transient collisional excitation scheme [35] (Fig. 1). The simulations consisted of three laser pulses, whose maxima arrived at 1.5, 2, and 2.51 ns from the start of the simulation, as depicted in Fig. 2. The temporal full width at half maximum (FWHM) values are, respectively, 1000, 100, and 0.5 ps. Both the timing and the pulse duration result from numerical optimization that aims to produce high gains during the best conditions for amplification (such as low electron-density gradients) [15]. The first pulse is used to create small weakly ionized plasma that facilitates the strong absorption of the energy of the second pulse, which is used to ionize the plasma. The last pulse instantaneously heats up the free electrons, dramatically increasing their kinetic energy and, therefore, the pumping rate.

All lasers had a super-Gaussian $I=I_0\exp[-y^2/(2\sigma^2)]^n$ spatial profile, with $n=10$, as suggested in [15]. The FWHM varied from 20 μm to 1 mm. In addition, an extreme case of a 2 mm width was studied and is presented separately in Sec. VI. For the sake of comparison, we kept the intensities constant for every plasma width at these values: 1.2×10^{11} W/cm^2 for the 1 ns pulse and 1.2×10^{12} and 1.1×10^{15} W/cm^2 for the 100 and 0.5 ps pulses, respectively. The laser wavelength was $\lambda=800$ nm. The target was an iron slab because the atomic properties and equations of state of iron are well known.

The results of the simulations and the postprocessing were 2D color maps (X-Y as shown in Fig. 3) of the different parameters of interest.

IV. COMPUTATIONAL RESULTS: HYDRODYNAMICS

As explained in Sec. III, simulations with different focal widths ranging from 20 μm to 1 mm were performed. Because we are interested in the energy extracted from the amplifier, the key parameters are gain and saturation fluence.

In Figs. 4, 2D false color maps of gain for different widths are shown. Figures 4(A) and 4(B) are magnified in Fig. 5 because gain zones are much smaller than the simulation window.

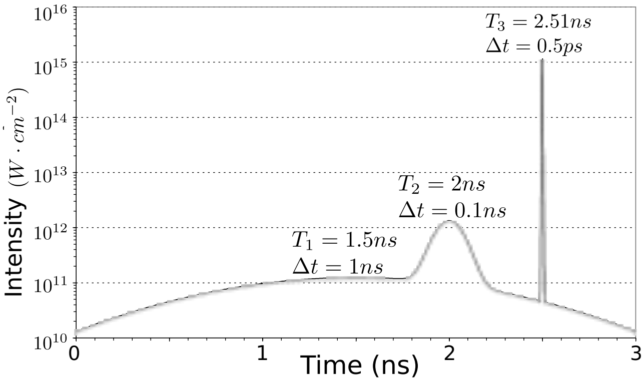

FIG. 2. Scheme of the simulations and the coordinate system used in the paper. HHG stands for *high harmonic generation* and indicates where the harmonics will be seeded in our scheme.

For a 20 μm width [Fig. 4(A)], we obtained a maximum gain of only 13 cm^{-1}. When we increased the FWHM of the laser from 20 to 30 μm (the width is multiplied by a factor of 1.5), the gain surprisingly increased to a maximum value of $g_0=60$ cm^{-1}, which is four times larger than the previous value of 13 cm^{-1}. For the 50 μm width plasma (now the width has been multiplied by a factor of 1.67), the gain was only 1.33 times larger than in the previous case ($g_0=80$ cm^{-1}). The next plasma used had a width of 75 μm and a maximum gain of $g_0=110$ cm^{-1} (width is multiplied by 1.5 and gain by 1.4). Finally, the gain achieved its maximum value of 126 cm^{-1} for a width of 100 μm [Fig. 4(E)]. Further increments of focal width did not increase the maximum gain value. In summary, a comparison of Figs. 4(A)–4(H) reveals a dramatic influence of the focal width on the peak gain value. Focal width also has a strong impact on the shape of the gain zone itself. We have observed that, in narrow plasmas (20 and 30 μm), there is a strong nonlinear correlation between the plasma width and the gain. On the other hand, in wider plasmas (100 μm, 150 μm, 200 μm, and 1 mm) the maximum gain is independent of the width. There are some *transition* plasmas (50 and 75 μm) where correlations appear between width and gain, but they are not as strong as in the narrowest cases.

In the Y direction there are also striking differences: the narrower plasmas (20 and 30 μm) present a much lower vertical (Y) extension of the gain zone (16 and 11 μm, respectively) that increases until 32, 42, and 51 μm for the 50, 75, and 100 μm, respectively, whereas the widest plasmas (150 μm, 200 μm, and 1 mm) have greater values com-

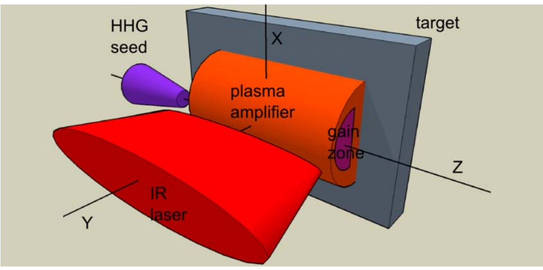

FIG. 3. (Color online) Scheme of the three laser pulses used in our simulations. The first pulse creates weakly ionized plasma. The second pulse is the main pulse, which creates the Ne-like ions. The third one is used to quickly increase the electron temperature. The X and Y axes represent the time and intensity in a logarithmic scale.

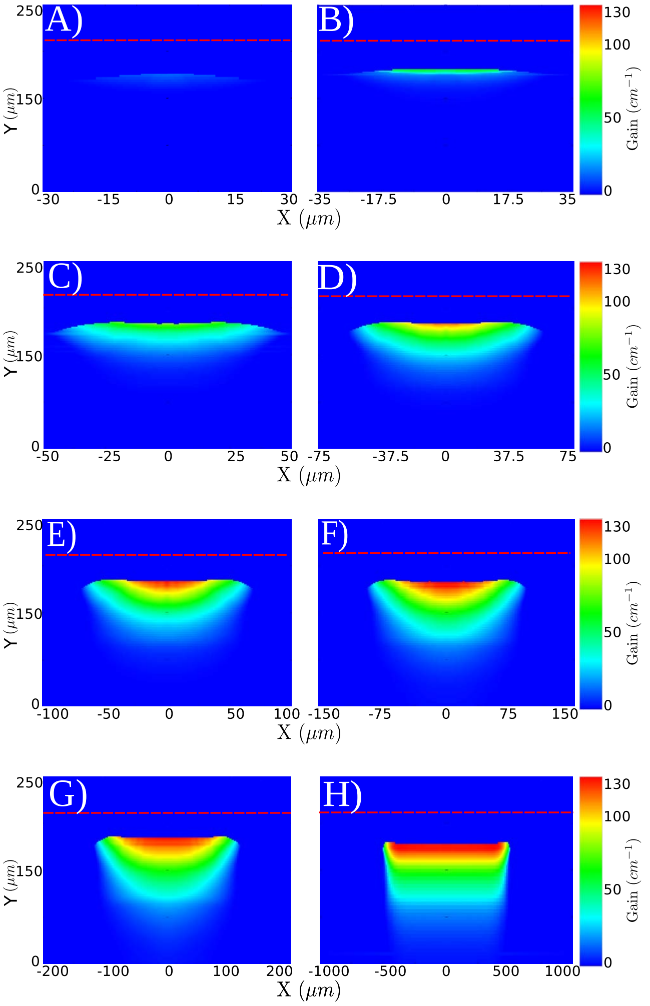

FIG. 4. (Color online) Gain maps in false colors for all simulated cases: 20 μm (A), 30 μm (B), 50 μm (C), 75 μm (D), 100 μm (E), 150 μm (F), 200 μm (G), and 1 mm (H) focal widths. All figures have the same vertical scale for convenience of comparison. The dashed red line indicates the initial position of the target. The pump lasers come from the bottom to the top (see Fig. 2).

pared with the narrower plasmas. Among the widest plasmas, similar values for vertical extension, around 70 μm at the center of the plasma ($X=0$ μm), are found.

In addition, it can be observed in Fig. 5 that the gain zone has a horizontal extension of about 34 μm in both cases, which is 1.7 times wider than the laser focal width in the 20 μm case. This is a surprising effect, keeping in mind that we use a super-Gaussian laser profile, which should reduce the lateral expansion, as explained in [15]. In Fig. 4, we can observe the same effect (gain zone being wider than the laser focal width) for 50, 75, and 100 μm plasmas, which have gain zones of 1.52, 1.33, and 1.2 times wider than the laser width, respectively. For 150 and 200 μm plasmas [Figs. 4(F) and 4(G)], the gain zone width almost matches the laser focal width (1.13 and 1.1 times wider), thus indicating that this effect is less pronounced in wider plasmas. Finally, in Fig. 4(H) the effect is not observed at all. In conclusion, we observe that not only the expansion in the Y axis but also the lateral expansion in the X axis play a role in focal width gain evolution, widening the gain zone in the cases where these 2D effects are strong (i.e., in narrower plasmas). For wider plasmas, these 2D effects do not affect the majority of the gain zone because their behavior is one dimension. All of these values are summarized in Table I.

According to the changes in the behavior of gain with the plasma width, three different regimes have been identified. The first relates to the narrowest plasmas (focal width ≤ 30 μm), with low gain, a small extension in the Y direction, and a gain zone that is much wider than the laser focal width (20 and 30 μm). The second regime relates to the widest plasmas (focal width ≥ 150 μm), with high gain, a large and similar extension in the Y direction, and a gain zone that tends to be as wide as the laser focal width. The third regime is intermediate between the first two.

These differences in lateral and vertical extension confirm that hydrodynamic processes have some importance in the development of gain. Creation of gain (an atomic process) is linked with the expansion of the plasma (a hydrodynamic process) via 9. Indeed, gain is proportional to the populations of the levels involved in the transition, as shown in Eq. (11), which depend on the electron-density squared (ion density varies with electron density). Then an increase of 1.4 in electron density (which is the density observed in plasmas with widths between 20 and 30 μm) will lead to a gain that is twice as larger. Nevertheless, the gain increases four times in this case. In conclusion, not only the changes in electron density but also the electron temperature via collisional excitation rates are important. Electron density and temperature are hydrodynamic parameters and, therefore, are strongly affected by evolution of the plasma.

In Fig. 6, 2D maps of electron temperature and electron-density isocontours at the moment of peak gain are shown.

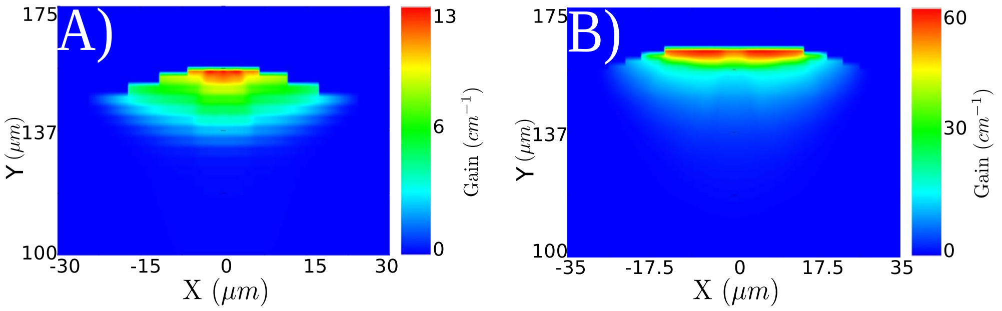

FIG. 5. (Color online) 2D false color gain maps for the 20 (left) and 30 μm (right) plasma cases, magnified from Figs. 4(A) and 4(B), respectively.

TABLE I. Gain zone parameters for the eight cases studied.

Width (μm)	20	30	50	75	100	150	200	1000
Gain (cm^{-1})	13	60	80	110	124	126	126	126
X length (μm)	34	36	76	100	120	170	220	1000
Y length (μm)	16	11	32	42	51	70	80	76
N_e ($\times 10^{20}$ cm^{-3})	0.63	0.9	1.3	1.9	2.2	2.2	2.4	2.4
T_e (eV)	311	531	491	524	531	531	529	536

We observe that the narrower the plasma, the lower the electron density in the gain region, being 6.7×10^{10} cm^{-3} for the 20 μm case and 0.9×10^{20} cm^{-3} for the 30 μm case, which represents an increment of 1.4 times the value of the 20 μm case. The electron density continues to increase very rapidly with focal width (1.3×10^{20}, 1.9×10^{20}, and 2.2×10^{20} cm^{-3} for 50, 75, and 100 μm widths), whereas wider plasmas have the same values of electron density (around 2.3×10^{20} cm^{-3}). In addition, the same effect appears for electron temperature, starting with 311 eV for the 20 μm case and increasing to 531 and 524 eV for the 30, 50, and 75 μm widths, respectively. Finally, it stabilizes around 530 eV for the widest plasma widths. Consequently, for the narrowest plasmas, gain cannot take place except in the small zone of relatively high density ($N_e > 5\times 10^{19}$ cm^{-3}) and high temperature ($T_e \approx 500$ eV). For larger plasmas, conditions suitable for gain exist in larger areas (as seen in Figs. 4 and 6).

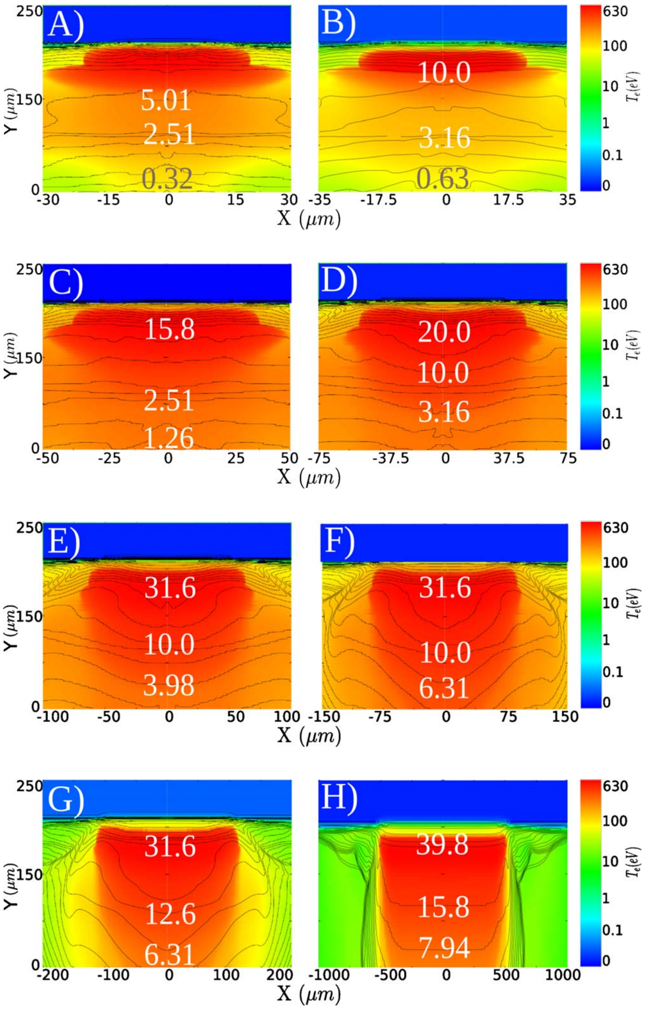

FIG. 6. (Color online) Electron temperature maps in false colors and electron-density isocontours for all simulated cases: 20 μm (A), 30 μm (B), 50 μm (C), 75 μm (D), 100 μm (E), 150 μm (F), 200 μm (G), and 1 mm (H) focal widths. The values of electron density are shown in white ($\times 10^{19}$ cm^{-3}). The pump lasers come from the bottom to the top.

In addition, we observed that, for Figs. 6(A)–6(D), density isocontours are approximately parallel to the X axis. In Fig. 6(E), curvature appears, which is clearly visible in Figs. 6(F) and 6(G), indicating that lateral electron-density gradients are present. This effect is enhanced in Fig. 6(H), where these lateral electron-density gradients (X direction) are clearly visible. These gradients confine a one-dimensional (1D) zone, which only expands in the Y direction and reduces the lateral thermal conduction. This explains the confinement of the gain in the width of the laser for the 1 mm plasma.

The differences observed in electron density, temperature, and behavior are very striking, as the intensities of the lasers are the same for all cases and, thus, have self-similar behaviors. As expected, this is observed at the center of the wider plasmas. The differences in temperature might be explained by taking into account two mechanisms: thermal conduction and laser absorption. Thermal conduction depends on electron-density gradients. In Fig. 6, it can be observed that there are no lateral gradients for the 20 and 30 μm width plasmas [Figs. 6(A) and 6(B)]. These lateral gradients start to develop in Figs. 6(C), 6(D), and 6(F) and are clearly observed in the rest of the figures, especially in Fig. 6(H).

The second effect directly linked with electron density is laser absorption via the inverse bremsstrahlung process [Eq. (17)],

$$\kappa_{ib}(\mathrm{cm}^{-1}) \approx 3.4\frac{(n_e/n_c)^2 Z \ln \Lambda}{\sqrt{1-n_e/n_c}\,\lambda^2_{\mu\mathrm{m}}(kT_e)^{3/2}_{\mathrm{keV}}}. \qquad (17)$$

In this formula, n_c is the critical density of the plasma, Z is the ionization, λ is the laser wavelength, and $\ln \Lambda$ is the Coulomb logarithm.

The low electron-density values ($n_e < 1.0\times 10^{20}$ cm^{-3}) of the narrowest plasmas (20 and 30 μm widths) prevent deposition of laser energy in regions of the plasma away from the critical density, reducing both the temperature and therefore the gain extension in the Y direction. Thus, the differences in observed behavior are driven by the electron density. However, electron density is not affected by the short pumping

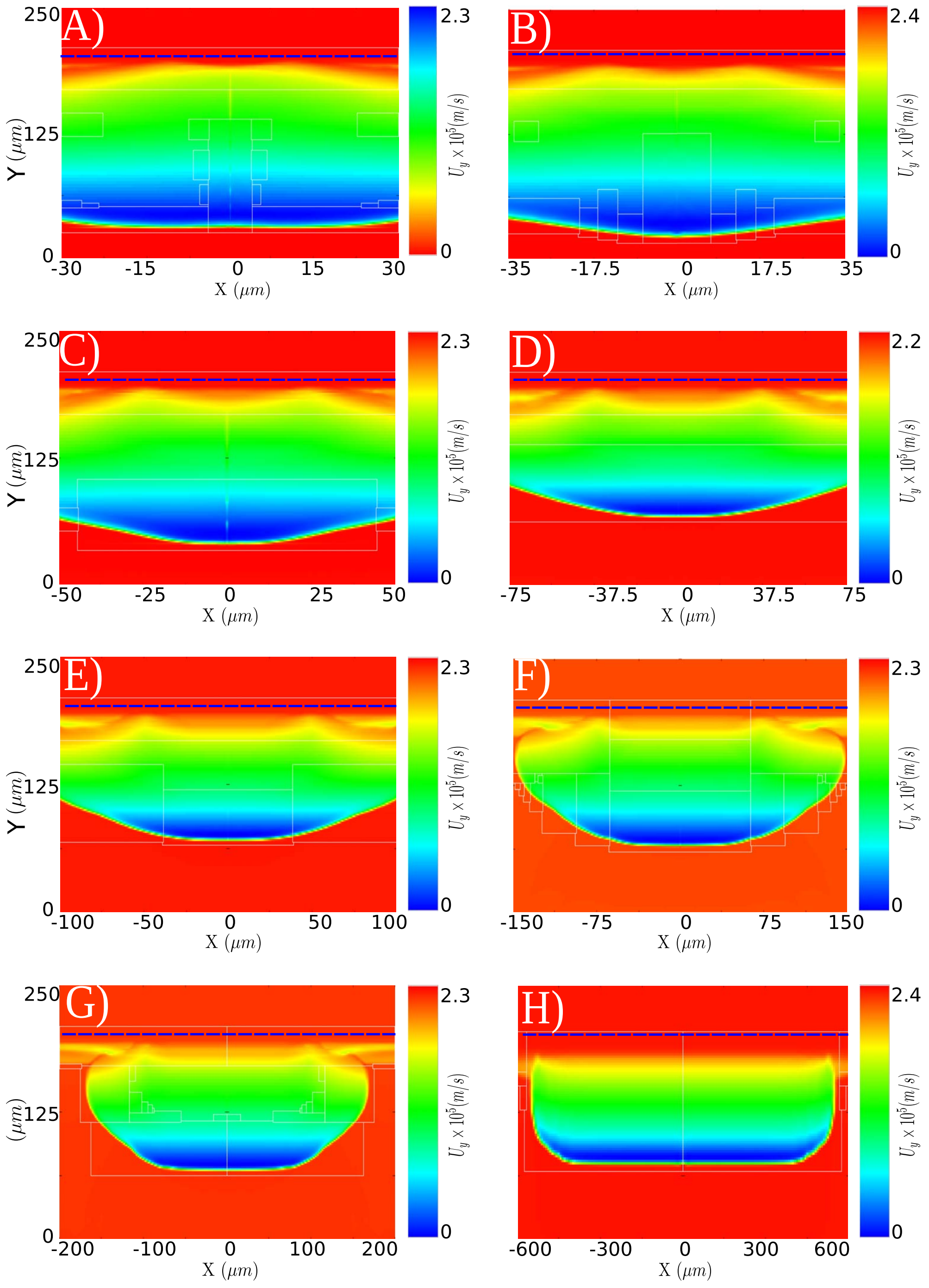

FIG. 7. (Color online) False color vertical velocity maps at $t=1.5$ ns for all eight plasma cases. The dashed blue line indicates the initial position of the target. The plasma expands downward.

pulse, which only increases the energy of the plasma free electrons. The departure from similarity observed in electron-density profiles in the narrowest plasmas must have started at earlier stages in the evolution of the plasmas.

The plasma expands mainly in the Y direction. This expansion usually determines electron-density gradients. In Fig. 7, 2D maps of vertical velocity at $t=1.5$ ns are shown. At first glance, we cannot appreciate the three different regimes already identified in Fig. 4. A more detailed study of the vertical velocities gives an average vertical velocity of $v_y \approx (2.3 \pm 0.1) \times 10^5$ m/s. In addition, these maximum values are attained in the low-density zones shown in blue in Fig. 7, which cover similar areas in all cases.

Then, this departure from similarity should be linked with lateral expansion in the plasma, which is suggested by the lateral wings in the gain regions for smaller plasmas (Fig. 4) and the curvature of density isocontours (Fig. 6).

In Fig. 8, the plasma's horizontal velocities at $t=1.5$ ns (i.e., the moment when the peak of the prepulse arrives) are shown. It is clearly seen in Figs. 8(A) and 8(B) that the fluid around the center of the plasma starts or has already started to expand laterally (the velocity around the center is non-

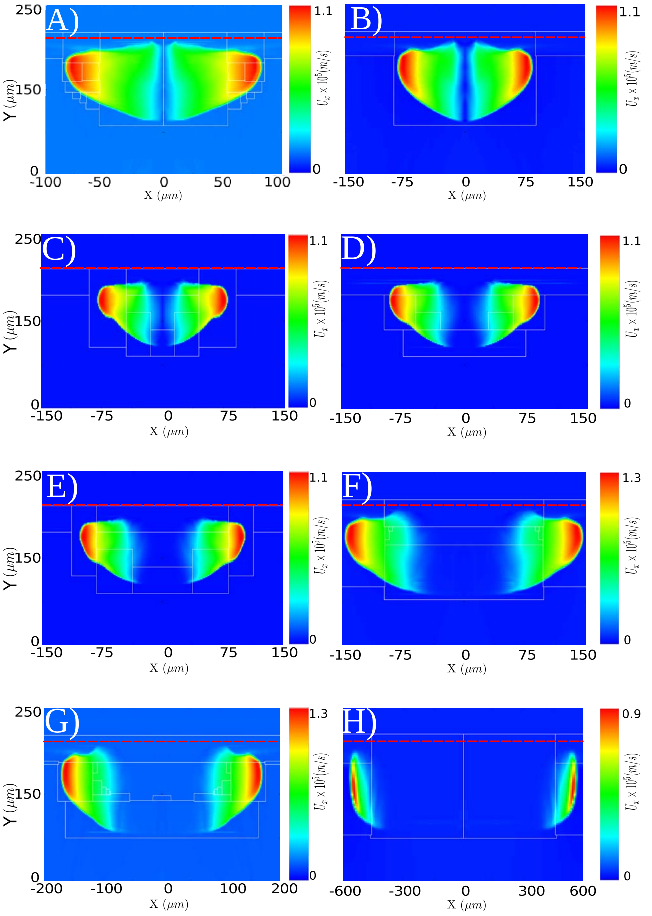

FIG. 8. (Color online) False color plasma velocity maps in the X direction at $t=1.5$ ns for all eight simulated cases. The horizontal scales are different in the 20 μm, 200 μm, and 1 mm cases.

zero). This lateral expansion lowers the electron density from the moment it reaches the center of the plasma until gain is produced ($\Delta t \approx 1$ ns in this case), which explains the low density of the narrower plasmas and the horizontal homogeneity we found. The maximum velocity for these cases is 1.1×10^5 m/s.

On the other hand, for the 150 μm, 200 μm, and 1 mm cases at $t=1.5$ ns [Figs. 8(F)–8(H)], the fluid at the center of the plasma only expands vertically (i.e., horizontal velocity is zero). The central region has a 1D behavior because the horizontal expansion can be approximated as an adiabatic rarefaction wave (see [39]). The horizontal extension of the rarefaction wave is determined by the position of the so-called *head* and *tail* of the rarefaction. The position of these points depends on the properties (horizontal velocity and sound speed) of the two states between when the expansion takes place. In our case, while self-similar behavior is still happening, the horizontal velocities of the two states involved are zero (the two states are the plasma center, which only expands vertically, and the surrounding vacuum). The sound speeds during the self-similar stage are the same for each case. Then the size of the region expanding horizontally is the same for all cases at the same time. For example, at $t=1.5$ ns, the size is about 85 μm, as shown in Fig. 8. The expanding region will increment as explained above until the tail of the rarefaction reaches the center of the plasma, as shown in Figs. 8(A) and 8(B). Then the parameter of interest is the sound speed at the center of the plasma because it will define the time when the rarefaction wave arrives at the center or the amount of plasma that has been accelerated horizontally when the pumping pulse arrives. In these cases, the maximum velocities found are 1.3×10^5, 1.3×10^5, and 0.9×10^5 m/s.

These two cases are the extremes, i.e., the cases where the adiabatic rarefaction wave has arrived at the center of the plasma at early stages [Figs. 8(A) and 8(B)] and the widest cases, where there is a wide unaffected region at the center of the plasma, which expands vertically until gain is created [Figs. 8(F)–8(H)]. The intermediate cases, shown in Figs. 8(C)–8(E), present a central zone that is not affected by the rarefaction at $t=1.5$ ns. Nevertheless, this zone is small and will be affected by the lateral expansion before gain is produced, explaining the differences in Fig. 4. The maximum value of velocity found in these intermediate cases is 1.1×10^5 m/s.

Now, we can explain the effects observed in Figs. 4 and 6. The prepulse accelerates the plasma in all cases. The plasma starts to expand laterally, independently of the plasma focal width. At $t=1.5$ ns, the lateral expansion arrives at the center of the 30 μm plasma, as shown in Fig. 8 (for the 20 μm plasma, the expansion arrives earlier, and for wider plasmas it will arrive later). Its behavior will no longer be similar to that of the wider cases, as the density at the center starts to decrease not only from the Y expansion but also from this X expansion. Thermal conduction is enhanced, transporting energy from the center to the rest of the plasma, reducing the temperature in the gain zone. When the pumping laser pulse arrives, the electron density is very low, reducing collisional pumping. Therefore, gain can only be created in a small region near the target's surface. In addition to this, the laser energy will be absorbed in a very small region near the critical density because inverse bremsstrahlung depends strongly on electron density (17), explaining the small extension in the Y direction of the gain zone in the narrowest cases. This same effect appears in the 50, 75, and 100 μm cases, but it occurs later than in the 30 μm case and is therefore less pronounced.

The 150 μm, 200 μm, and 1 mm widths evolve similarly at the center of the plasma because the horizontal acceleration has not arrived there yet when gain is created. This is why these three cases have the same electron-density profiles (Fig. 6) and the gains have the same extension in the Y direction [Figs. 4(F)–4(H)]. However, at $t=2.54$ ns, when the gain is created, the region with $U_x \neq 0$ (plasma velocity in the X direction) is not negligible for the 150 μm and the 200 μm cases. Then electron densities and gain isocontours are curved. This is not the case with the 1 mm width plasma. The region horizontally accelerated is still negligible at the moment when population inversion takes place. We observe a large, hot, dense, 1D zone that is confined by the horizontal electron-density gradient where gain takes place. All these hydrodynamic data are summarized in Table I.

V. COMPUTATIONAL RESULTS: AMPLIFICATION

Now we consider the processes of seeding and amplifying the high harmonics inside the plasma. Modeling the amplifi-

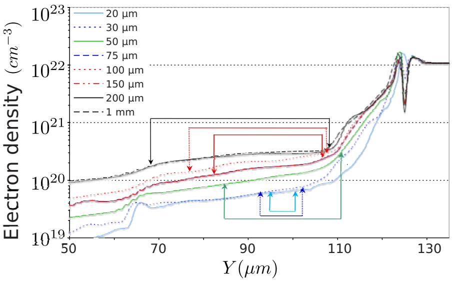

FIG. 9. (Color online) Electron density profiles in the Y direction at the center of the plasma ($X=0$ μm) for the eight cases studied. The plasmas expand from right to left. The initial position of the target is $Y=200$ μm. The extensions of the gain regions are indicated by colored arrows. Note that there is only one set of arrows (the longest one) for the three widest cases (1 mm, 200 μm, and 150 μm plasmas).

cation of the seeded beam is a difficult task as the amplified beam may suffer a strong refraction [6] in addition to the well-known issue of spectral coupling with the lasing line [7,8,14]. This last point will be discussed later in this section. We will first consider the question of beam propagation in plasmas having different degrees of homogeneity, depending on the focal width (Fig. 4). Prior to any calculation of beam propagation, it is interesting to estimate, as a zeroth step, the energy available to be extracted in a single pass by the high harmonics seeded inside the plasma. Equation (18) represents an upper limit of the energy that can be extracted, although less energy will be obtained experimentally. This parameter E_{avail} (see [40,41]) is useful for comparing the efficiencies of the different amplifiers,

$$E_{avail} = (\ln G_0)E_{sat} = g_0 \cdot l \cdot E_{sat}, \tag{18}$$

$$G_0 = \exp g_0 l, \tag{19}$$

$$E_{sat} = F_{sat} \cdot \Delta x \cdot \Delta y, \tag{20}$$

where F_{sat}, the saturation fluence, is obtained by solving Eq. (10) with our simple atomic physics calculation. Δx and Δy are the spatial extensions of the gain zone along the X and Y directions.

A rough calculation of the maximum distance that a seeded beam could propagate without exiting the gain region due to refraction was performed. We will use this estimation as the length, l, needed to calculate E_{avail} in Eq. (18). The lateral deflection of a beam propagating in an inhomogeneous plasma of length l is given by Eq. (21) (see [42]), assuming linear transverse electron-density gradients

$$\Delta Y(\mu m) \approx 2.24 \times 10^{-26} l^2(\text{cm})\lambda_{\text{XUV}}^2 \nabla_y n_e, \tag{21}$$

where λ_{XUV} is the wavelength (in Å) of the seeded ray and $\nabla_y n_e$ is the vertical electron-density gradient in cm^{-4}. We use as ΔY the length of the gain zone in the Y direction and the average electron-density gradient in the gain region indicated in Fig. 9. We can compute the maximum length until the beam is refracted out of the gain zone. The results for $\lambda_{\text{XUV}}=25.5$ nm are summarized in Table II. We observe an important variation in the propagation length versus the plasma width. For the narrowest plasma (20 μm focal width), the propagation length is about 13 mm, although it drops to 6.3 mm for a plasma with a 30 μm focal width. This might be understood by looking at Fig. 6, which shows a strong lateral flow for 20 μm that trends to smooth out the lateral gradient. This flow diminishes for the plasma with a 30 μm focal width, leading to an enhanced density gradient. For larger focii, the density gradients stay nearly constant around values of $(1.5-2.4)\times 10^{22}$ cm^{-4}. However, the enlargement of the focal width enables the propagation of the beam for longer distances (from 10.9 to 16.7 mm).

Similar calculations have been done using the horizontal electron-density gradient $\nabla_x N_e$. Nevertheless, refraction in the X direction is less important than in the Y direction in most cases, as it is shown in Table II. The narrowest plasmas (with 20 and 30 μm widths) are homogeneous in the X direction due to the lateral expansion. The widest plasmas (with 200 μm and 1 mm widths) present a large plateau of the electron density because the refraction in the X direction is negligible. For the rest of the cases, refraction in the Y direction is more restrictive. This is logical as we are using super-Gaussian focusing, so lateral electron-density gradients are expected to diminish, as explained in [15].

We then computed the saturation energy by multiplying the saturation fluence (10), given by our atomic model, by the area of the gain region. In the 30 μm case, the gain zone surface is about 36×8 μm^2 along the X and Y directions, respectively. Our atomic model gives a saturation fluence of about $F_{sat}=2.3$ mJ/cm^2. As the gain zone has a surface of about 2.9×10^{-6} cm^2, we can estimate the saturation energy as $E_{sat}\approx 6.6$ nJ. The maximum energy available in the plasma is given by Eq. (18). Any energy in the range (E_{sat}, E_{avail}) can be extracted by increasing the plasma length after saturation has been reached. In Table III, we summa-

TABLE II. Electron density gradients and maximum lengths until refraction pushes the beam out of the gain zone. The subindex in the length indicates which derivative has been used to compute it. The 20 and 30 μm plasma cases does not present any lateral gradients, and the 200 μm and 1 mm plasmas present a plateau of the electron density.

Width (μm)	20	30	50	75	100	150	200	1000
$(\nabla_y N_e)_{x=0}$ ($\times 10^{22}$ cm^{-4})	0.65	1.9	1.8	1.6	2.4	1.8	2.0	2.1
Length Y (mm)	13	6.3	10.9	13.6	12	16.5	16.7	15.8
$(\nabla_x N_e)_{y=cnt}$ ($\times 10^{22}$ cm^{-4})			0.86	1.9	1.7	1.4		
Length X (mm)			14.1	11.5	14.1	19		

TABLE III. Energy of the long and short pulse lasers, maximum length the injected seed can travel through the plasma, gain, saturation fluence, saturation energy, extracted energy, maximum energy available for extraction, and pumping efficiency.

Width (μm)	E_{in}^{ns} (J)	E_{in}^{ps} (J)	L_y (mm)	Gain (cm^{-1})	F_{sat} (mJ/cm^2)	E_{sat} (μJ)	E_{avail} (μJ)	E_{out} (μJ)	Eff (μJ/J)
20	0.75	1.75	13	13	2.2	1×10^{-3}	0.017	0.01	4×10^{-3}
30	0.24	0.56	6	60	2.3	6×10^{-3}	0.25	0.06	8×10^{-2}
50	0.3	0.7	11	80	2.4	6×10^{-2}	6	0.6	0.6
75	0.33	0.77	13	110	2.5	0.11	16	1.1	1.0
100	0.39	0.91	12	124	2.5	0.15	22	1.5	1.1
150	0.57	1.33	16	126	2.6	0.31	65	3.1	1.6
200	0.78	1.82	17	126	2.6	0.46	97	4.6	1.8
1000	4.0	9.2	16	126	2.6	2.2	447	22	1.7

rized the saturation fluencies and thus the energies for every cases studied in this paper. It is interesting to note that the saturation fluence evolves very slowly with the laser focal widths. An increase of only 20% exists between the narrowest case of a 20 μm plasma (2.2 mJ/cm^2) to the largest case of a 1 mm plasma (2.61 mJ/cm^2). This is logical because saturation fluence depends only on the stimulated emission cross section, σ [Eq. (15)]. In our calculations, this has as its only varying parameter the ion temperature (16), which does not change significantly from one line focus to another. However, our model takes into account only Doppler broadening while collisional broadening should also be treated. Collisional broadening will not induce any major changes, but it will slightly reduce the gain. Consequently, longer plasmas are required to achieve the same amplification level and, therefore, a more energetic pump laser is needed. However, increasing the spectral width induces an enhancement in saturation fluence (9) and (10) that will lead to a higher output energy. Finally, these two effects would probably counterbalance each other, making our calculation valid for a general understanding and estimate of the energy that may be extracted from different plasmas. A new version of the atomic model will take into account collisional broadening and introduce some dependency with the electron density.

Figure 4 was derived from the extraction of the surface of the different gain regions and shows the resulting estimated saturation energies. The different values are reported in Table III. We observed a strong relationship between E_{sat} and the focal width that comes from the variation of the amplifying region surface. For the narrowest plasma (20 μm), the saturation energy is as low as 1 nJ, but it rises quickly to 6.6 nJ for a plasma with a 30 μm focal width, 64 nJ for a plasma with a 50 μm width (i.e., a ten times enhancement for only a 50% enlargement of the focal width), and up to 0.1 μJ for a 75 μm width plasma. This rise in saturation energy is nearly linear with the plasma width since the plasma starts to have a dominantly 1D expansion. For a 1 mm plasma width, a saturation energy as high as 2.2 μJ has been estimated.

With our estimations of maximum amplification lengths and saturation energies, we can compute the available energies as shown in Table III. From these values, it is observed that increasing the plasma width from 30 to 50 μm induces a change in the available energy from $E_{avail}=0.25$ μJ to $E_{avail}=5.6$ μJ, which is more than 20 times the value of the 30 μm plasma. Increasing this energy by 75 and 100 μm increments increases it to $E_{avail}=16.5$ μJ and $E_{avail}=22.3$ μJ, which is an increase proportional to the increase in width (both width and E_{avail} are multiplied by 1.25). A new unexpected increment appears in the 150 μm case. The width is multiplied by 1.5, but the available energy increases by three times that ($E_{avail}=65.1$ μJ). Then the energy is proportional to the width in the rest of the cases. $E_{avail}=97.4$ μJ for a plasma with a 200 μm width (width and energy are multiplied by 1.33) and $E_{avail}=447$ μJ for a plasma with a 1 mm width (a factor of 5). The 1 mm plasma represents a strikingly interesting amplifier for achieving output energy near or above 100 μJ, i.e., above any subpicosecond soft-x-ray sources currently available in laboratories.

The three different regimes, where energy increases proportionally with the plasma width are separated by sudden increases in the available energy. The 20 μm case is particularly interesting because, despite the high amplification length, the product $g_0 \cdot l = 16.9$ does not reach the saturation value ($g_0 \cdot l \approx 18$, as stated in [43]) due to the very low small-signal gain. Consequently, it seems that very narrow plasmas are not good amplifiers.

As mentioned above, the available energy has an asymptotic limit. Experimentally, increasing the plasma length far above saturation is interesting for extracting the stored energy but requires higher energy pump lasers. Since any energy between E_{sat} and E_{avail} is reachable, we benchmarked our results according to recent seeding experiments. In [7], the measured total output energy was 38 times higher than the saturation energy. In this paper, we will assume a more conservative value for the output energy equal to ten times the saturation energy, as observed in [43].

Then, for a 20 μm focal width, the output energy is about 10 nJ, reaching 66 nJ for a 30 μm width, which is in very good agreement with the maximum energy of 50–60 nJ measured in [8]. Our modeling (75 μm focal width) also agrees very well with experiments performed by Lindau *et al.* [44] and Cassou *et al.* [45] but with an unseeded soft-x-ray laser. A direct comparison of energy and fluence is still valid since it has been demonstrated by Guilbaud *et al.* [46] that this soft-x-ray laser emits only a few trains of pulse.

Again, we observed three regimes: 20–30 μm focal widths with output energies below 100 nJ; 50–100 μm

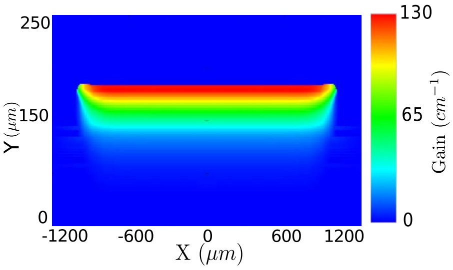

FIG. 10. (Color online) False color Gain map for a 2 mm wide plasma. The laser comes from the bottom to the top of the picture.

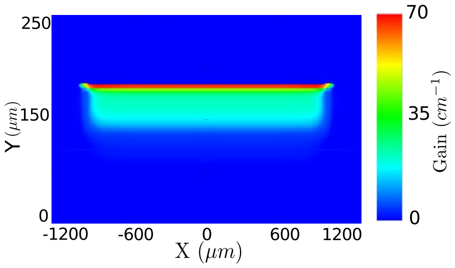

FIG. 11. (Color online) False color gain map for a 2 mm wide plasma created by using a pumping pulse with half the intensity of the ones used in the rest of simulations.

widths with quickly increasing energies from 0.6 to 1.5 μJ, and then from 150 μm to 1 mm widths the energy follows the focal width; and from 3 up to 22 μJ. The amount of energy that can be easily extracted is comparable to the energy achieved in FLASH free-electron lasers [47], which is to date the most intense coherent soft-x-ray laser source.

To evaluate the pumping efficiency, we estimated the plasma length necessary to achieve an amplification factor of 1000 with respect to the seed beam energy. This value corresponds to a strong but still realistic amplification [8,10]. Since the high harmonic generation (HHG) spectral width is assumed to be 100 times larger than the soft-x-ray laser focal width, the amplification at the line center has to be 10^5. For a 20 μm width, the length for achieving this amplification is nearly 9 mm, but it drops to 2 mm for the 30 μm width plasma, with the consequence of a huge decrease in pumping energy. It increases gradually again for larger plasmas due to the higher amount of matter that is needed to heat up. Thus, the net pumping energies are 2.5 J for a 20 μm plasma and 2 and 13 J for 150 μm and 1 mm plasmas, respectively. The pumping efficiency rises strikingly from 4 nJ/J for the narrower plasma up to 1590 and 1710 nJ/J for the 150 μm and 1 mm plasmas, respectively.

VI. COMPUTATIONAL RESULTS: TOWARD WIDER PLASMAS

We have demonstrated that wider plasmas enhance the properties of the gain zone and optimize the energy that can be extracted from the amplifier. Then a question arises: with sufficient pumping energy (up to hundreths of joules), how much energy can we extract from wider and wider plasmas? As explained, the evolution of the plasma will be self-similar at least until the lateral expansion arrives at the center of the plasma. For the timing used in this paper, this is ensured for plasmas wider than 150 μm. In Fig. 10, the gain region for a 2 mm wide plasma, using the same laser intensities as in the other cases, is shown. As expected, we obtain a smooth 1D gain region with a maximum value of about 130 cm^{-1} in a 2 mm wide plasma. The saturation energy is 4.45 μJ and, therefore, the extracted energy is 44 μJ (the available energy is $E_{avail}=821$ μJ). With a density gradient of $\nabla Ne_y=2.8\times10^{22}$ cm^{-4}, the length until refraction deviates the seed beam out of the gain region is 14.2 mm. The energy used to create and pump the plasma is $E=26$ J. Nevertheless, there is a substantial difference between this case and the former ones. Now, the transverse length (the plasma width) is not negligible, and the transverse gain-length product is $g_0 \cdot l=26$ (not taking into account saturation effects), which is above the common saturation values ($g_0 \cdot l \approx 18$ [43]). Saturated transverse lasing will appear, depopulating the lasing levels and reducing the extracted energy. In conclusion, there exists a limit to the increase of the plasma width that is independent of the available pumping energy. In this preliminary study, we considered the limit to be given by keeping the ASE at a level that is 100th below the saturation energy, i.e., for a $g_0 \cdot l$ value of 1415.

As gain is proportional to the intensity of the pumping pulse, one way to overcome this problem is to reduce the intensity of the picosecond pulse. In Fig. 11, we show the gain map of a 2 mm plasma that has been pumped with a pulse that has half the intensity of the former case (i.e., $I=5.8\times10^{14}$ $\mathrm{W/cm}^2$). The prepulse and the main pulse are the same as for the rest of the cases.

The reduction of the gain to $g_0=70$ cm^{-1} at the maximum leads to a transverse gain length of $g_0 \cdot l=14$. The intensity for $g_0 \cdot l=14$ is 55 times below the saturation intensity and, therefore, transverse lasing is extracting only a negligible part of the energy stored in the plasma. Although the saturation fluence in both cases is the same (as it depends only on ion temperature), the reduction of the gain surface also reduces the saturation energy ($E_{sat}=3.2$ μJ) and extracted energy ($E_{out}=32$ μJ). In addition, the reduction of gain will result in an increase in the amplifier length to saturate and extract the maximum energy possible, going from 0.8 mm in the former case to 1.6 mm. This is not a problem because the energy used to create the plasma will be $E_{\mathrm{ns}}=13.18$ J in the prepulse and main pulse and $E_{\mathrm{ps}}=16$ J in the short pulse, with a total energy of $E=29.18$ J. This is not so different from the former case, which had an efficiency of 1096 nJ/J, which is less than that in the 1 mm case but still above that in the narrower cases. The length until refraction is, in this case, 1.95 cm.

In conclusion, reducing the intensity of the main pulse inhibits transverse lasing at the cost of increasing the length of the plasma needed to obtain the same E_{out} and lowering the efficiency but still at achievable values. The conditions of the gain zone are still very good for seeding and amplifying.

VII. CONCLUSIONS

We have performed a full numerical study of different transient collisional excitation (TCE) plasmas using 2D hydrodynamic simulations, continuing the work of earlier studies [15,48]. We confirmed the crucial role of using 2D hydrodynamic codes for ensuring the correct description of the physical parameters of the plasma amplifier. We used the 2D hydrodynamic code with radiation transport in AMR ARWEN [17] and postprocessed the data obtained with a three-level atomic model to study the $2p^5_{1/2}3s_{1/2}\ J=1\rightarrow 2p^5_{1/2}3p_{1/2}\ J=0$ neonlike Fe^{16+} transition at 25.5 nm.

Our results have been validated with experiments from Wang *et al.* [8,9] and Cassou *et al.* [45], obtaining values of gain, saturation fluence, and electron density where population inversion takes place in good agreement with experimental values. Our model suggests that, for Wang's experiment, the gain zone is very small because of deleterious hydrodynamical effects and, therefore, the output energy is intrinsically limited to values below 100 nJ. Simulations performed with wider plasmas corroborate this assumption. The lateral expansion at early stages of plasma evolution can be treated as a rarefaction between two states (the center of the plasma and the surrounding vacuum). Consequently, all plasmas will present self-similar behavior. This statement is valid until the rarefaction arrives at the center of the plasma, which happens early on in the narrowest plasmas (the arrival time depends on the sound velocity at the center of the plasma, which is the same for all the cases during self-similar behavior). At that moment, the electron density at the center is reduced by the lateral expansion, inhibiting the mechanism that creates the population inversion (electron collisional excitation) and thus reducing the gain coefficient and the extension of the gain region. For wider plasmas, the lateral expansion cannot reach the central region before gain occurs. Thus, a geometry is proposed, requiring an increase in the width and a decrease in the length of the plasma so as to extract more energy and to dramatically increase the pumping efficiency. With this geometry, energies as high as 22 μJ can be obtained with a 1 mm wide plasma.

Transverse lasing will appear when the product gain width approximates the saturation value because this is the limit (and not the driving laser energy) of the widths that can be used. Nevertheless, reducing the intensity of the pumping pulse will inhibit transverse lasing while conserving the good amplification properties of the wider plasmas.

Energies up to 100 μJ could be obtained with this scheme. Lasers with enough energy to create these wide plasmas will be available in a few years, so this would be a huge step forward for seeded soft-x-ray lasers.

ACKNOWLEDGMENTS

The authors would like to acknowledge the financial support provided by the LASERLAB II 228334 (SFINX) European Project and RTRA "Triangle de la Physique" project (SHYLAX) and the Spanish Ministerio de Educación y Ciencia within the Program No. ENE2009-09837/FTN.

[1] R. E. Burge, M. T. Browne, P. Charalambous, G. E. Slark, and P. J. Smith, Opt. Lett. **18**, 661 (1993).

[2] J. Itatani, J. Levesque, D. Zeidler, H. Niikura, H. Pépin, J. C. Kieffer, P. B. Corkum, and D. M. Villeneuve, Nature (London) **432**, 867 (2004).

[3] H. Wabnitz, A. R. B. de Castro, P. Gurtler, T. Laarmann, W. Laasch, J. Schulz, and T. Moller, Phys. Rev. Lett. **94**, 023001 (2005).

[4] H. N. Chapman, Nature Mater. **8**, 299 (2009).

[5] B. Rus, T. Mocek, A. R. Präg, M. Kozlová, G. Jamelot, A. Carillon, D. Ros, D. Joyeux, and D. Phalippou, Phys. Rev. A **66**, 063806 (2002).

[6] T. Ditmire, M. H. R. Hutchinson, M. H. Key, C. L. S. Lewis, A. MacPhee, I. Mercer, D. Neely, M. D. Perry, R. A. Smith, J. S. Wark, and M. Zepf, Phys. Rev. A **51**, R4337 (1995).

[7] P. Zeitoun, G. Faivre, S. Sebban, T. Mocek, A. Hallou, M. Fajardo, D. Aubert, P. Balcou, F. Burgy, D. Douillet, S. Kazamias, G. de Lachèze-Muriel, T. Lefrou, S. le Pape, P. Mercère, H. Merdji, A. S. Morlens, J. P. Rousseau, and C. Valentin, Nature (London) **431**, 426 (2004).

[8] Y. Wang, E. Granados, F. Pedaci, D. Alessi, B. M. Luther, M. Berrill, and J. J. Rocca, Nat. Photonics **2**, 94 (2008).

[9] Y. Wang, E. Granados, M. A. Larotonda, M. Berrill, B. M. Luther, D. Patel, C. S. Menoni, and J. J. Rocca, Phys. Rev. Lett. **97**, 123901 (2006).

[10] N. Hasegawa, T. Kawachi, A. Sasaki, M. Kishimoto, K. Sukegawa, M. Tanaka, R. Z. Tai, Y. Ochi, M. Nishikino, K. Nagashima, and Y. Kato, Phys. Rev. A **76**, 043805 (2007).

[11] F. Pedaci, Y. Wang, M. Berrill, B. Luther, E. Granados, and J. J. Rocca, Opt. Lett. **33**, 491 (2008).

[12] Y. Wang, M. Berrill, F. Pedaci, M. M. Shakya, S. Gilbertson, Z. Chang, E. Granados, B. M. Luther, M. A. Larotonda, and J. J. Rocca, Phys. Rev. A **79**, 023810 (2009).

[13] J. P. Goddet, S. Sebban, J. Gautier, P. Zeitoun, C. Valentin, F. Tissandier, T. Marchenko, G. Lambert, M. Ribières, D. Douillet, T. Lefrou, G. Iaquaniello, F. Burgy, G. Maynard, B. Cros, B. Robillard, T. Mocek, J. Nejdl, M. Kozlova, and K. Jakubczak, Opt. Lett. **34**, 2438 (2009).

[14] D. S. Whittaker, M. Fajardo, P. Zeitoun, J. Gautier, E. Oliva, S. Sebban, and P. Velarde, Phys. Rev. A **81**, 043836 (2010).

[15] K. Cassou, P. Zeitoun, P. Velarde, F. Roy, F. Ogando, M. Fajardo, G. Faivre, and D. Ros, Phys. Rev. A **74**, 045802 (2006).

[16] E. Oliva, P. Zeitoun, S. Sebban, M. Fajardo, P. Velarde, K. Cassou, and D. Ros, Opt. Lett. **34**, 2640 (2009).

[17] F. Ogando and P. Velarde, J. Quant. Spectrosc. Radiat. Transf. **71**, 541 (2001).

[18] F. Ple, M. Pittman, G. Jamelot, and J.-P. Chambaret, Opt. Lett. **32**, 238 (2007).

[19] B. Zielbauer, D. Zimmer, J. Habib, O. Gilbaud, S. Kazamias, M. Pittman, and D. Ros, Appl. Phys. B: Lasers Opt. **100**, 731 (2010).

[20] P. Velarde, F. Ogando, S. Eliezer, J. Martínez-Val, J. Perlado, and M. Murakami, Laser Part. Beams **23**, 43 (2005).

[21] P. Velarde, D. García-Senz, E. Bravo, F. Ogando A. R. Relaño, C. García, and E. Oliva, Phys. Plasmas **13**, 092901 (2006).

[22] P. Colella and H. M. Glaz, J. Comput. Phys. **59**, 264 (1985).

[23] R. E. Ewing, *Multigrid Methods* (SIAM, Philadelphis, 1987).

[24] S. Chandrasekhar, *Radiative Transfer* (Dover Publications, New York, 1960).

[25] K. D. Lathrop, Nucl. Sci. Eng. **24**, 381 (1966).

[26] R. M. More, K. H. Warren, D. A. Young, and G. B. Zimmerman, Phys. Fluids **31**, 3059 (1988).

[27] E. Minguez and R. Falquina, Laser Part. Beams **10**, 651 (1992).

[28] M. J. Berger and P. Colella, J. Comput. Phys. **82**, 64 (1989).

[29] C. A. Rendleman, V. E. Beckner, M. Lijewski, W. Crutchfield, and J. B. Bell, Comput. Visualization Sci. **3**, 147 (2000).

[30] C. for Computational Science and Engineering (unpublished).

[31] S. L. Pape and P. Zeitoun, Opt. Commun. **219**, 323 (2003).

[32] Y. Li and G. P. Preztler, Phys. Plasmas **4**, 164 (1997).

[33] B. L. Whitten, A. U. Hazi, M. H. Chen, and P. L. Hagelstein, Phys. Rev. A **33**, 2171 (1986).

[34] W. H. Goldstein, B. L. Whitten, A. U. Hazi, and M. H. Chen, Phys. Rev. A **36**, 3607 (1987).

[35] P. V. Nickles, V. N. Shlyaptsev, M. Kalachnikov, M. Schnurer, I. Will, and W. Sandner, Phys. Rev. Lett. **78**, 2748 (1997).

[36] T. Shirai, Y. Funatake, K. Mori, J. Sugar, W. L. Wiese, and Y. Nakai, J. Phys. Chem. Ref. Data **19**, 127 (1990).

[37] J. A. Koch, B. J. MacGowan, L. B. Da Silva, D. L. Matthews, J. H. Underwood, P. J. Batson, R. W. Lee, R. A. London, and S. Mrowka, Phys. Rev. A **50**, 1877 (1994).

[38] H. V. Regemorter, Astrophys. J. **136**, 906 (1962).

[39] E. F. Toro, *Riemann Solvers and Numerical Methods for Fluid Dynamics* (Springer-Verlag, Berlin, 1999).

[40] P. W. Milonni and J. H. Eberly, *Lasers* (Wiley, New York 1988).

[41] A. E. Siegman, *Lasers* (University Science Books, California, 1986).

[42] G. J. Pert, Plasma Phys. **25**, 387 (1983).

[43] J. Dunn, Y. Li, A. L. Osterheld, J. Nilsen, J. R. Hunter, and V. N. Shlyaptsev, Phys. Rev. Lett. **84**, 4834 (2000).

[44] F. Lindau, O. Lundh, A. Persson, K. Cassou, S. Kazamias, D. Ros, F. Plé, G. Jamelot, A. Klisnick, S. de Rossi, D. Joyeux, B. Zielbauer, D. Ursescu, T. Kühl, and C.-G. Wahlström, Opt. Express **15**, 9486 (2007).

[45] K. Cassou, S. Kazamias D. Ros, F. Plé, G. Jamelot, A. Klisnick, O. Lundh, F. Lindau, A. Persson, C.-G. Wahlström, S. de Rossi, D. Joyeux, B. Zielbauer, D. Ursescu, and T. Kühl, Opt. Lett. **32**, 139 (2007).

[46] O. Guilbaud, F. Tissandier J. Goddet, M. Ribíre, S. Sebban, J. Gautier, D. Joyeux, D. Ros, K. Cassou, S. Kazamias, A. Klisnick, J. Habib, P. Zeitoun, D. Benredjem, T. Mocek, J. Nedjl, S. de Rossi, G. Maynard, B. Cros, A. Boudaa, and A. Calisti, Opt. Lett. **35**, 1326 (2010).

[47] V. Ayvazyan, N. Baboi, J. Bähr, V. Balandin, B. Beutner, A. Brandt, I. Bohnet, A. Bolzmann, R. Brinkmann, O. Brovko, J. Carneiro, S. Casalbuoni, M. Castellano, P. Castro, L. Catani, E. Chiadroni, S. Choroba, A. Cianchi, H. Delsim-Hashemi, G. D. Pirro, M. Dohlus, S. Düsterer, H. Edwards, B. Faatz, A. Fateev, J. Feldhaus, K. Flöttmann, J. Frisch, L. Fröhlich, T. Garvey, U. Gensch, N. Golubeva, H.-J. Grabosch, B. Grigoryan, O. Grimm, U. Hahn, J. Han, M. Hartrott, K. Honkavaara, M. Hüning, R. Ischebeck, E. Jaeschke, M. Jablonka, R. Kammering, V. Katalev, B. Keitel, S. Khodyachykh, Y. Kim, V. Kocharyan, M. Körfer, M. Kollewe, D. Kostin, D. Krämer, M. Krassilnikov, G. Kube, L. Lilje, T. Limberg, D. Lipka, F. Löhl, M. Luong, C. Magne, J. Menzel, P. Michelato, V. Miltchev, M. Minty, W. Möller, L. Monaco, W. Müller, M. Nagl, O. Napoly, P. Nicolosi, D. Nölle, T. N. nez, A. Oppelt, C. Pagani, R. Paparella, B. Petersen, B. Petrosyan, J. Pflüger, P. Piot, E. Plönjes, L. Poletto, D. Proch, D. Pugachov, K. Rehlich, D. Richter, S. Riemann, M. Ross, J. Rossbach, M. Sachwitz, E. Saldin, W. Sandner, H. Schlarb, B. Schmidt, M. Schmitz, P. Schmüser, J. Schneider, E. Schneidmiller, H.-J. Schreiber, S. Schreiber, A. Shabunov, D. Sertore, S. Setzer, S. Simrock, E. Sombrowski, L. Staykov, B. Steffen, F. Stephan, F. Stulle, K. Sytchev, H. Thom, K. Tiedtke, M. Tischer, R. Treusch, D. Trines, I. Tsakov, A. Vardanyan, R. Wanzenberg, T. Weiland, H. Weise, M. Wendt, I. Will, A. Winter, K. Wittenburg, M. Yurkov, I. Zagorodnov, P. Zambolin, and K. Zapfe, Eur. Phys. J. D **37**, 297 (2006).

[48] E. Oliva, P. Zeitoun, M. Marti, P. Velarde, M. Fajardo, and K. Cassou, J. Phys.: Conf. Ser. **112**, 042066 (2008).